

Variable stars in the bulge globular cluster NGC 6401

Y. Tsapras^{1,7}, A. Arellano Ferro², D.M. Bramich³, R. Figuera Jaimes^{4,5}, N. Kains⁶,
R. Street⁷, M. Hundertmark^{8,5}, K. Horne⁵, M. Dominik⁵, C. Snodgrass^{9,10}
(Affiliations can be found after the references)

Draft June 2016

ABSTRACT

We present a study of variable stars in globular cluster NGC 6401. The cluster is only 5.3° away from the Galactic centre and suffers from strong differential reddening. The photometric precision afforded us by difference image analysis resulted in improved sensitivity to variability in formerly inaccessible interior regions of the cluster. We find 23 RRab and 11 RRC stars within one cluster radius ($2.4'$), for which we provide coordinates, finder-charts and time-series photometry. Through Fourier decomposition of the RR Lyrae star light curves we derive a mean metallicity of $[\text{Fe}/\text{H}]_{\text{UVES}} = -1.13 \pm 0.06$ ($[\text{Fe}/\text{H}]_{\text{ZW}} = -1.25 \pm 0.06$), and a distance of $d \approx 6.35 \pm 0.81$ kpc. Using the RR Lyrae population, we also determine that NGC 6401 is an Oosterhoff type I cluster.

Key words: Globular Clusters: NGC 6401 – Variable Stars: RR Lyrae.

1 INTRODUCTION

Globular clusters are gravitationally bound stellar systems which, for the most part, contain between 10^5 to 10^6 stars in a volume spanning a few hundred parsecs. These systems are home to some of the oldest stellar populations in the Galaxy and are rich in variable stars of the RR Lyrae type, which are particularly useful for obtaining distance measurements. There are currently 158 globular clusters associated with the Milky Way for which there exist estimates of their distance, metallicity, age and dynamical parameters (Harris 1996).

This paper belongs to a series of studies of variable stars in globular clusters (e.g. Arellano Ferro et al. (2015); Kains et al. (2015); Arellano Ferro et al. (2013); Figuera Jaimes et al. (2013); Bramich et al. (2011)) aimed primarily at Fourier decomposing the light curves of RR Lyrae stars in search of physical parameters and at updating the variability census using modern instruments and photometric reduction methods. In particular, the combination of modern CCDs and the technique of difference image analysis (Alard & Lupton 1998; Bramich 2008) allow us to probe for variability closer to the crowded central regions of the clusters than was previously possible.

Globular cluster NGC 6401 (also known as GCL1735-238 and ESO520-SC11) is located at equatorial coordinates $(\alpha, \delta)_{J2000} = (17^{\text{h}}38^{\text{m}}37^{\text{s}}, -23^{\circ}54'32'')$ and galactic coordinates $(l, b) = (3.45^\circ, +3.98^\circ)$, only 5.3° from the Galactic centre. According to the 2010 update to the Harris (1996) catalogue, it is a relatively metal rich cluster ($[\text{Fe}/\text{H}] \approx -1.02$ dex) with an estimated distance from the Sun of $d_\odot \approx 10.6$ kpc. However, the metallicity estimate is contradicted by studies done by Davidge (2001) and Valenti, Ferraro & Origlia (2007), who derive metallicities of $[\text{Fe}/\text{H}] \approx -1.5$ and $[\text{Fe}/\text{H}] \approx -1.37$ dex respectively. They conclude that the cluster appears to be metal poor.

The paper is structured as follows: In section 2, we give an account of our observations and data reduction methods. Section 3 contains a description of our methodological approach to identifying and classifying variable sources in the vicinity of NGC 6401. In section 4 we provide an account of the Fourier decomposition of the light curves of the RR Lyrae stars and how the derived parameters are used to estimate the physical properties of the cluster. We comment on our results in section 5 and conclude in section 6.

2 OBSERVATIONS AND REDUCTIONS

2.1 Observations

Observations of the target field were a by-product of the RoboNet microlensing campaign (Tsapras et al. 2009) and were obtained in the campaign-specific SDSS- g' and SDSS- i' bands throughout the months of July and August 2013 using the LCOGT¹ 1m robotic telescope network. The LCOGT telescopes are clones of each other, featuring identical instruments, and are deployed in clusters of two to three at the Siding Spring Observatory (SSO), South African Astronomical Observatory (SAAO) and Cerro Tololo Inter-American Observatory (CTIO). The detectors used were standard SBIG STX-16803, with 4096×4096 pixels, each $0.23''$, giving a field of view of $15.8' \times 15.8'$. Image binning was set to 2×2 , giving an effective pixel scale of $0.47''$. A summary of the observations can be found in table 1.

¹ www.lcogt.net

Table 1. The distribution of observations of NGC 6401 for each filter, where the columns N_g and N_i represent the number of images taken in the SDSS- g' and SDSS- i' bands respectively. We also provide the exposure time(s) employed during each night for each filter in the columns t_g and t_i .

Date	N_g	t_g (s)	N_i	t_i (s)
20130705	—	—	2	200
20130707	—	—	8	200
20130708	—	—	7	200
20130711	—	—	4	200
20130712	—	—	1	200
20130717	—	—	4	200
20130721	41	60-200	48	60-200
20130722	8	60-200	4	60
20130724	21	60-200	29	60-200
20130725	39	60-200	41	60-200
20130726	34	60-200	22	60-200
20130727	40	60-200	43	60-200
20130728	13	60-200	39	60-200
20130729	22	60-200	39	60-200
20130730	19	60-200	18	60-200
20130731	25	60-200	27	60-200
20130801	27	60-200	32	60-200
20130802	9	60-200	12	60-200
20130803	22	60-200	10	60-200
20130804	22	60-200	18	60-200
20130805	14	60-200	20	60-200
20130808	2	60	4	60-200
20130809	39	60-200	36	60-200
20130810	16	60-200	23	60-200
20130811	12	60-200	18	60-200
Total:	425		509	

2.2 Difference Image Analysis

Using our DanDIA² pipeline (Bramich et al. 2013), we performed difference image analysis (DIA) on the images to extract high-precision photometric measurements. Since all images were obtained from a network of identical telescopes, all images taken with the same filter were processed together, regardless of which telescope they originated from.

At the first step, every image underwent standard debiasing and flat-fielding calibrations. Subsequently, a reference (template) image was constructed for each filter by combining a set of registered best-seeing images obtained with the same instrument. For each reference image we measured the fluxes and positions of all PSF-like objects (stars) by extracting a spatially variable empirical PSF from the image and fitting this PSF to each detected object. Image registration was performed using the triangle matching method of Pal & Bakos (2006) to match the stars detected in each image with those detected in the reference, and then deriving a linear transformation between the images that uses cubic O-MOMS resampling (Blu et al. 2001). In this way, all images were geometrically aligned to match the relevant reference.

Difference images were generated by subtracting the relevant reference image, convolved with an appropriate spatially variable kernel, from each registered image. The spatially variable convolution kernel was determined using bilinear interpolation of a set of kernels, modelled as discrete pixel arrays (Bramich 2008), that were derived for a uniform 13×13 grid of subregions across the image.

Difference fluxes for each star detected in the reference image were evaluated from each difference image by using fixed position PSF photometry. Light curves were constructed by calculating the

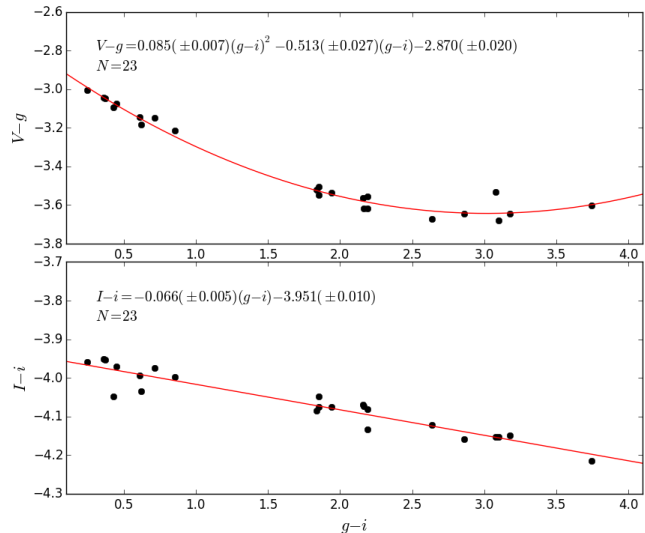


Figure 1. Transformation relations between the instrumental and the standard photometric systems using a set of standard stars in the field of NGC 6401 provided by Peter Stetson.

total flux $f_{\text{tot}}(t)$ in ADU/s at each epoch t using:

$$f_{\text{tot}}(t) = f_{\text{ref}} + \frac{f_{\text{diff}}(t)}{p(t)} \quad (1)$$

where f_{ref} is the reference flux (ADU/s), $f_{\text{diff}}(t)$ is the differential flux (ADU/s) and $p(t)$ is the photometric scale factor (the integral of the kernel solution).

To convert to instrumental magnitudes, we used:

$$m_{\text{ins}}(t) = 25.0 - 2.5 \log [f_{\text{tot}}(t)] \quad (2)$$

where $m_{\text{ins}}(t)$ is the instrumental magnitude of the star at time t . Uncertainties were propagated in the appropriate analytical fashion.

The above procedure and its caveats have been described in detail in Bramich et al. (2011) and the interested reader is referred there for relevant details.

2.3 Photometric Calibrations

2.3.1 Relative

Systematic errors in photometric measurements are caused by a whole range of effects such as mismatches between the true and measured flat-field calibrations, insufficiently accurate modelling of the spatially varying PSF, poor image subtractions in DIA, etc. These types of errors affect all light curves to a greater or lesser extent dependent on the data properties and photometry algorithms employed. Although it is not possible to suppress them completely, it is often the case that substantial qualitative improvements can be made when dealing with time-series photometry (e.g. Bramich et al. (2015); Kains et al. (2015)). We used the method from Bramich & Freudling (2012) to determine the magnitude offsets Z_k that should be applied to each photometric measurement from the image k , which translates into a correction for any systematic errors introduced into the DIA photometry due to errors in the fitted photometric scale factors $p(t)$. The offsets derived were of order ~ 1 -2% for the SDSS- g' band, and somewhat smaller for the SDSS- i' band. The application of this correction substantially improved the quality of the light curves.

² DanDIA is built from the DanIDL library of IDL routines available at <http://www.danidl.co.uk>

2.3.2 Absolute

We identified 23 standard stars in the field of NGC 6401 from the online collection of Stetson (2000)³ which we used to transform instrumental (g, i) magnitudes into the standard (V, I) system. Our derived transformations are depicted in Figure 1. For the i -band we obtained a linear relation, as expected, since the SDSS- i' band is similar to the Johnson-Cousins I -band. However, for the observations in the g -band, we obtained a non-linear (quadratic) relation. This is due to the fact that the SDSS- g' band is bluer than the Johnson-Cousins V -band (Ivezic et al. 2007). Furthermore, NGC 6401 is heavily affected by differential reddening which is more evident in the bluer bands. The analytical transformations used for the calibration are as follows:

$$V_{std} = g + 0.085(\pm 0.007)(g - i)^2 - 0.513(\pm 0.027)(g - i) - 2.870(\pm 0.020), \quad (3)$$

$$I_{std} = i - 0.066(\pm 0.005)(g - i) - 3.951(\pm 0.010). \quad (4)$$

It is important to note that while these transformations shift the instrumental magnitudes to the V and I magnitude scales, the fact that the photometry pertains to the g and i -bands remains unchanged. Hence the transformations do not affect the overall shape/amplitude of the light curves for the variable stars in our sample, and the light curves we present are simply g and i -band light curves on the standard V and I brightness scale.

Once these transformations were applied to the light curves, we proceeded to generate the colour-magnitude diagram (CMD) shown in Figure 2 using the inverse-variance-weighted mean V and I magnitudes for 23698 stars identified in our images. Blue and green filled circles mark the relevant locations on the diagram for the cluster RRab and RRc stars respectively (see section 3). The plot shows an almost vertical main sequence (MS) between magnitudes 15 to 20, which is mostly due to contamination from foreground stars in the Galactic disk. The red horizontal branch (RHB) is the concentration of stars at $V \sim 18$, which is mixed with the fainter end of the red giant branch (RGB). The tilted RGB extends to magnitude $V - I \sim 5 - 6$. Some differential reddening is present, indicated by the tilt and elongation of the RHB and RGB.

To validate the transformations, we compare our calibrated magnitudes with a set of 1041 photometrically calibrated OGLE stars from the field BLG626.24 in the vicinity of NGC 6401⁴ and find that for the majority of these stars the magnitudes match to within ~ 0.06 mag.

2.4 Astrometry

We used the GAIA (Draper et al. 2000) image display tools to derive a linear astrometric solution for the SDSS- g' filter reference image by matching 1429 stars from the UCAC4 star catalogue (Zacharias 2012). After manually rejecting saturated stars and stars at the edges of the image we achieved a radial RMS scatter in the residuals of $\sim 0.22''$. Similarly, for the SDSS- i' filter we used 1528 stars from the UCAC4 catalogue and obtained an RMS of $\sim 0.25''$. The astrometric fit was then used to calculate the J2000.0 celestial coordinates for all of the confirmed variables in our field of view (see Tables 3 and 4).

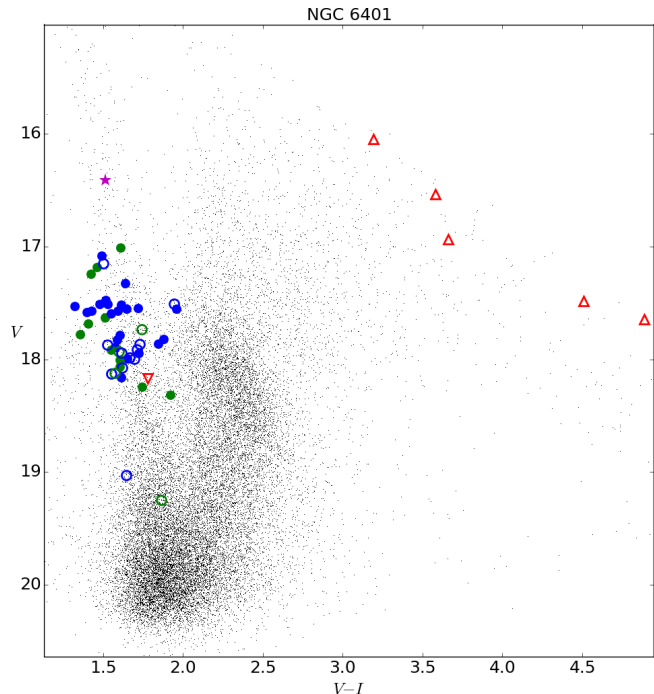


Figure 2. Colour-magnitude diagram of NGC 6401. Blue and green filled circles mark the cluster RRab and RRc stars respectively. Unfilled circles represent non-cluster RR Lyraes. The triangles on the top right are long period variables NSV09307, NSV09288, LPV9, LPV10 and LPV11. The purple star marks the location of V3. The inverted red triangle on the middle-left of the plot ($V \sim 18.1$) is variable E1.

3 VARIABLE STARS IN NGC 6401

A series of searches for variable stars at and around NGC 6401 conducted in the '70s by Terzan & Rutily (1972, 1973, 1975) yielded 25 variables (labelled V1-25) that could be cluster members⁵. They are listed in the Clement et al. (2001) catalogue in the January 2015 update⁶. However, detailed studies of these variables were never published.

The first observations of this cluster using CCDs were performed by Barbuy et al. (1999), who observed for a single night (July 4, 1998) with the 1.5m Danish telescope at ESO (La Silla). Although theirs was not a search for variables, they performed PSF-fitting photometry with Daophot II (Stetson 1987) on their images and used their CMD diagrams to estimate the amount of reddening and the cluster's distance from the Sun.

NGC 6401's proximity to the Galactic bulge places it in the fields monitored by the fourth phase of the Optical Gravitational Lensing Experiment (OGLE) survey which started operations in 2011 (Udalski et al. 2015). Soszynski et al. (2014) present a comprehensive collection of ~ 38000 RR Lyrae stars detected over 182 square degrees monitored by the OGLE-IV survey in the densest regions of the Galactic bulge. Of those, ~ 300 are identified as plausible members of 15 globular clusters. Their list includes 31 RR Lyrae stars lying within one cluster angular radius from the centre of NGC 6401, several of which were previously unknown. Their photometric reductions were performed using the OGLE real time

⁵ They also identified a large number of variable star candidates in our field of view that are not cluster members, but we have not been able to recover any of them in our search.

⁶ <http://www.astro.utoronto.ca/~cclement/cat/C1735m238>

³ www3.cadc-ccda.hia-ihp.nrc-cnrc.gc.ca/community/STETSON/standards

⁴ The OGLE light curves were kindly provided by Igor Soszynski.

Table 2. Time-series SDSS- g' and SDSS- i' photometry, linearly transformed to the V and I bands respectively, for all of the confirmed variables in our field of view. The standard M_{std} and instrumental m_{ins} magnitudes are listed in columns 4 and 5, respectively, corresponding to the variable star, filter, and epoch of mid-exposure listed in columns 1-3, respectively. The uncertainty on m_{ins} is listed in column 6, which also corresponds to the uncertainty on M_{std} . For completeness, we also list the quantities f_{ref} , f_{diff} and p from Equation 1 in columns 7, 9 and 11, along with the uncertainties σ_{ref} and σ_{diff} in columns 8 and 10. This is an extract from the full table, which is available with the electronic version of the article.

Variable Star ID	Filter	HJD (d)	M_{std} (mag)	m_{ins} (mag)	σ_m (mag)	f_{ref} (ADU s^{-1})	σ_{ref} (ADU s^{-1})	f_{diff} (ADU s^{-1})	σ_{diff} (ADU s^{-1})	p
V2	g	2456495.20657	18.024	21.286	0.145	34.473	0.924	-6.838	7.218	1.7640
V2	g	2456495.21746	17.956	21.218	0.110	34.473	0.924	-3.424	5.963	1.8019
⋮	⋮	⋮	⋮	⋮	⋮	⋮	⋮	⋮	⋮	⋮
V2	i	2456479.64343	16.088	20.099	0.011	103.089	2.051	-24.881	1.968	2.1117
V2	i	2456479.74302	16.186	20.196	0.020	103.089	2.051	-12.404	0.994	0.6315
⋮	⋮	⋮	⋮	⋮	⋮	⋮	⋮	⋮	⋮	⋮

Table 3. Details for all confirmed RR Lyrae stars within one cluster radius ($2.4'$) from the NGC 6401 cluster centre. Period estimates for each variable from this work are reported in column 4 and from previous studies in column 5 for comparison. Mean magnitudes are reported in columns 8 and 9 and peak-to-peak amplitudes in columns 10 and 11. The epoch reported in column 12 is the light curve maximum.

Variable Star ID	OGLE ID	Variable Type	OGLE		RA (J2000.0)	Dec (J2000.0)	$\langle V \rangle$ (mag)	$\langle I \rangle$ (mag)	A_g (mag)	A_i (mag)	Epoch (HJD-2450000)
			Period (days)	Period (days)							
V2	OGLE-BLG-RRLYR-24004	RRab	0.70158	0.70235	17:38:33.97	-23:54:26.6	17.66	15.94	0.93	0.48	6500.9323
V4	OGLE-BLG-RRLYR-24049	RRab	0.47233	0.47248	17:38:36.36	-23:54:35.2	—	—	1.18	—	6499.2669
V5	OGLE-BLG-RRLYR-24006	RRab	0.53289	0.53386	17:38:34.01	-23:54:40.8	18.23	16.39	1.19	0.64	6514.9621
V6	OGLE-BLG-RRLYR-24078	RRab	0.44446	0.44417	17:38:38.19	-23:53:58.2	17.96	16.37	1.55	0.91	6507.3248
V7	OGLE-BLG-RRLYR-24126	RRab	0.54563	0.54575	17:38:40.99	-23:54:32.3	17.60	16.00	1.19	0.62	6495.2935
V8	—	RRc	0.32485	—	17:38:38.72	-23:55:25.0	17.71	16.13	0.54	0.24	6508.3582
V9	OGLE-BLG-RRLYR-24055	RRab	0.51367	0.51311	17:38:36.76	-23:54:39.2	17.51	15.75	1.15	0.54	6505.9660
V10	—	RRab	0.52603	—	17:38:38.57	-23:53:52.4	17.88	16.20	1.32	0.68	6503.5181
V11	OGLE-BLG-RRLYR-24121	RRab	0.58212	0.58183	17:38:40.82	-23:54:08.2	17.59	16.00	0.90	0.46	6501.5939
V12	OGLE-BLG-RRLYR-24030	RRc	0.29130	0.29109	17:38:35.09	-23:54:30.8	17.23	15.73	0.67	0.34	6503.5043
V13	OGLE-BLG-RRLYR-24036	RRab	0.56498	0.56527	17:38:35.63	-23:54:49.0	18.04	16.31	1.13	0.59	6495.4983
V14	—	RRab	0.60851	—	17:38:39.37	-23:54:39.0	17.58	15.84	0.54	0.24	6495.3499
V15	OGLE-BLG-RRLYR-24075	RRab	0.50440	0.50644	17:38:37.78	-23:55:09.5	17.84	16.21	1.30	0.71	6499.2100
V16	OGLE-BLG-RRLYR-24043	RRab	0.50581	0.50552	17:38:36.00	-23:55:58.1	18.51	16.63	1.27	0.70	6505.5065
V17	OGLE-BLG-RRLYR-24131	RRab	0.50517	0.50524	17:38:41.67	-23:52:57.0	17.22	15.62	1.34	0.74	6501.7732
V18	OGLE-BLG-RRLYR-24002	RRab	0.56830	0.57021	17:38:33.84	-23:54:03.8	17.71	16.05	1.25	0.66	6499.5121
V19	OGLE-BLG-RRLYR-24160	RRab	0.55989	0.55949	17:38:43.80	-23:56:12.1	17.63	16.04	1.06	0.57	6507.4949
V21	OGLE-BLG-RRLYR-24056	RRc	0.27809	0.27814	17:38:36.77	-23:54:12.2	17.86	16.46	0.52	0.30	6507.9500
V22	OGLE-BLG-RRLYR-24025	RRc	0.29972	0.29971	17:38:34.87	-23:54:40.6	17.98	16.37	0.50	0.24	6499.2900
V23	OGLE-BLG-RRLYR-24100	RRc	0.36641	0.36647	17:38:39.91	-23:52:27.2	17.28	15.82	0.51	0.25	6501.0665
V24	OGLE-BLG-RRLYR-24182	RRab	0.52000	0.52013	17:38:45.53	-23:53:54.8	17.65	16.01	1.05	0.55	6507.9216
V25	OGLE-BLG-RRLYR-24047	RRab	0.55867	0.55860	17:38:36.27	-23:55:03.0	17.55	15.59	0.71	0.28	6504.6719
V26	OGLE-BLG-RRLYR-23926	RRab	0.49585	0.49683	17:38:28.16	-23:54:24.2	18.22	16.33	1.16	0.59	6509.9683
V27	OGLE-BLG-RRLYR-23985	RRc	0.28743	0.28783	17:38:33.01	-23:55:04.8	18.40	16.40	0.55	0.19	6503.4900
V28	OGLE-BLG-RRLYR-23999	RRab	0.62576	0.62373	17:38:33.56	-23:56:52.8	18.00	16.24	0.54	0.34	6499.5121
V29	OGLE-BLG-RRLYR-24011	RRc	0.28860	0.28856	17:38:34.16	-23:55:07.2	18.34	16.52	0.55	0.24	6503.0370
V30	OGLE-BLG-RRLYR-24021	RRc	0.26198	0.26207	17:38:34.79	-23:55:05.0	18.07	16.42	0.42	0.20	6498.4785
V31	OGLE-BLG-RRLYR-24024	RRab	0.57712	0.57840	17:38:34.87	-23:54:35.6	18.00	16.06	0.91	0.39	6495.4983
V32	OGLE-BLG-RRLYR-24037	RRab	0.66136	0.66059	17:38:35.65	-23:54:51.8	17.94	15.96	0.68	0.30	6495.2728
V33	OGLE-BLG-RRLYR-24039	RRc	0.34032	0.34087	17:38:35.70	-23:55:26.3	18.13	16.48	0.50	0.25	6503.6545
V34	OGLE-BLG-RRLYR-24060	RRab	0.54441	0.54533	17:38:36.79	-23:54:35.4	17.60	15.93	0.90	0.41	6505.6228
V35	OGLE-BLG-RRLYR-24062	RRc	0.28284	0.28300	17:38:37.00	-23:54:35.5	17.05	15.41	0.31	0.12	6501.6900
V36	OGLE-BLG-RRLYR-24142	RRc	0.31898	0.31905	17:38:42.86	-23:52:57.3	17.76	16.29	0.44	0.23	6500.5692
V37	OGLE-BLG-RRLYR-24148	RRab	0.47915	0.47961	17:38:43.06	-23:52:35.3	17.93	16.23	1.38	0.77	6500.0600

photometric pipeline (Udalski 2003), which is based on difference image analysis, and the final photometry of selected variables was calibrated to the standard VI system with an estimated zero-point accuracy of $\sim 0.02\text{mag}$.

3.1 Detection of new variable stars

Our pipeline generated 26727 and 31762 light curves for the stars measured in the SDSS- g' and SDSS- i' reference images respectively. We proceeded by compiling a list of known variables in a $16' \times 16'$ area centred on NGC 6401 using the equatorial co-

ordinates and finding charts available in the OGLE-IV database⁷ and the coordinates provided by Samus et al. (2009). We also considered long period variables in the General Catalog of Variable Stars (GCVS)⁸ (Samus et al. 2009) and the International Variable Star Index (VSX) of the American Association of Variable Star Observers (AAVSO)⁹.

In order to identify variable sources in our data, we employed

⁷ <ftp://ftp.astrouw.edu.pl/ogle/ogle4/OCVS/blg/rrlyr/>

⁸ <http://www.sai.msu.su/gcvs/gcvs/index.htm>

⁹ <https://www.aavso.org/vsx/>

Table 4. Details for all remaining confirmed variables in the field of NGC 6401. Period estimates for each variable from this work are reported in column 3 and from previous studies in column 4 for comparison. Mean magnitudes are reported in columns 7 and 8. The epoch reported in column 9 is the light curve maximum.

Variable Star ID	Variable Type	Period (days)	OGLE Period (days)	RA (J2000.0)	Dec (J2000.0)	$\langle V \rangle$ (mag)	$\langle I \rangle$ (mag)	Epoch (HJD-2450000)
V3	CWB	1.74869	—	17:38:41.31	-23:54:34.9	16.41	14.90	6497.9440
E1	EB	1.33228	—	17:38:37.42	-24:00:52.0	18.17	16.39	6495.4922
LPV1	LPV	—	—	17:38:41.02	-23:56:26.6	—	—	6495.4983
LPV2	LPV	—	—	17:38:36.89	-23:49:23.5	—	—	6509.6726
LPV3	LPV	—	—	17:38:36.35	-23:54:20.5	—	—	6509.2758
LPV4	LPV	—	—	17:38:33.28	-23:58:37.9	—	—	6498.5154
LPV5	LPV	—	—	17:38:31.02	-23:48:47.8	—	—	6501.7620
LPV6	LPV	—	—	17:38:29.84	-23:57:17.1	—	—	6503.5181
LPV7	LPV	—	—	17:38:23.66	-23:51:26.8	—	—	6507.5209
LPV8	LPV	—	—	17:38:18.85	-23:51:04.2	—	—	6501.7620
LPV9	LPV	—	—	17:38:15.93	-24:00:04.6	16.54	12.96	6514.6812
LPV10	LPV	—	—	17:38:12.37	-23:51:55.4	16.93	13.27	6516.5155
LPV11	LPV	—	—	17:38:08.05	-23:47:16.6	16.04	12.85	6514.4772
LPV12	LPV	—	—	17:38:41.74	-23:54:22.4	—	—	6495.2174
NSV 09288	LPV	—	—	17:38:02.73	-23:46:41.4	17.48	12.97	6514.4762
NSV 09307	LPV	—	—	17:38:17.70	-24:01:29.9	17.65	12.75	6495.5296
NSV 09349	LPV	—	—	17:38:46.09	-23:47:33.3	—	—	6503.5034
V2226 Oph	LPV	—	—	17:38:21.23	-23:50:43.7	—	—	6503.5181
V2227 Oph	LPV	—	—	17:38:21.80	-23:55:22.7	—	—	6516.5146
OGLE-BLG-RRLYR-23731	RRab	0.68325	0.68279	17:38:09.55	-24:01:35.9	17.87	16.34	6495.2390
OGLE-BLG-RRLYR-23799	RRab	0.52350	0.52347	17:38:16.60	-23:46:36.7	—	—	6495.3700
OGLE-BLG-RRLYR-23863	RRab?	0.68212	0.68160	17:38:22.97	-23:51:51.6	17.74	16.00	6498.5800
OGLE-BLG-RRLYR-23880	RRab	0.55167	0.55149	17:38:24.43	-23:51:49.2	17.98	16.32	6495.7350
OGLE-BLG-RRLYR-23969	RRc	0.32692	0.32682	17:38:31.63	-23:50:06.4	19.27	17.40	6495.8150
OGLE-BLG-RRLYR-24007	RRab	0.44022	0.43985	17:38:34.08	-23:59:28.3	19.03	17.38	6497.4737
OGLE-BLG-RRLYR-24026	RRab	0.50640	0.50689	17:38:34.89	-23:57:13.5	17.99	16.33	6495.1150
OGLE-BLG-RRLYR-24044	RRab	0.46785	0.46743	17:38:36.09	-23:50:17.5	18.02	16.30	6509.9880
OGLE-BLG-RRLYR-24050	RRc	0.36286	0.36284	17:38:36.46	-24:01:15.3	18.12	16.55	6501.9897
OGLE-BLG-RRLYR-24058	RRab	0.60849	0.60920	17:38:36.79	-23:51:51.3	17.87	16.14	6500.7392
OGLE-BLG-RRLYR-24066	RRab	0.51589	0.51623	17:38:37.43	-23:47:53.4	—	—	6500.6292
OGLE-BLG-RRLYR-24124	RRab	0.49729	0.49800	17:38:40.86	-23:51:59.3	17.15	15.66	6509.0082
OGLE-BLG-RRLYR-24138	RRc	0.31636	0.31635	17:38:42.60	-24:01:22.4	17.93	16.34	6507.7153
OGLE-BLG-RRLYR-24255	RRab	0.61989	0.61915	17:38:50.64	-23:54:11.7	17.51	15.57	6496.2955
OGLE-BLG-RRLYR-24293	RRab	0.53190	0.53177	17:38:53.97	-23:53:30.3	18.07	16.45	6496.2615
OGLE-BLG-RRLYR-24325	RRab	0.51808	0.51817	17:38:56.67	-23:56:19.0	18.13	16.58	6499.2784
OGLE-BLG-RRLYR-24383	RRab	0.61407	0.61420	17:39:02.24	-24:00:54.3	17.91	16.20	6504.9341

three different methods. Using all SDSS- g' band light curves, we performed a Lomb-Scargle (LS) periodogram search for periods between 0.1 to 1.3 days (method 1), retaining the best-fit periods. A subsequent second run with no restriction on the period was performed to identify variables that vary on longer timescales. For the same set of light curves, we also evaluated the \mathcal{S}_B variability statistic (method 2), as defined in equation 3 from Figuera Jaimes et al. (2013). Data points deviating more than three times the RMS error from the mean magnitude were clipped during this process. This removed between 0-4 data points from the light curves but mostly left them unaffected. Lastly, for each filter we constructed a ‘residual superimage’ by taking the absolute value of the residual ADU counts at each pixel (i, j) for every difference image and summing over the images (method 3). For a detailed description of the method, see Bramich et al. (2011). Variable sources were easier to spot with this method since their PSF-like peaks on the superimage were strongly enhanced.

To select candidate variable stars, we required $\mathcal{S}_B > 1.0$ and best-period LS Power score > 0.4 . These selection criteria were decided empirically by looking at the respective distributions of these parameters, and were intentionally set low enough so as to ensure no candidate variables were missed.

Upon visual inspection of the candidates, after removing duplicates and bad quality light curves, 62 were retained as showing genuine variability. Almost all previously known variables were identified by this procedure. However, we did not find any evidence of variability for any of the sources identified in the immedi-

ate vicinity of the coordinates of previously reported variables V1, V20, which were also not found in the OGLE variable database, and OGLE-BLG-RRLYR-23724. We note that the OGLE database also does not contain any variables in the reported coordinates of V3, V8, V10 and V14, all of which were identified by our analysis.

From the residuals superimages in each filter, we selected candidate variables by visually identifying all PSF-like objects. We then examined the light curves corresponding to the coordinates of these objects and identified 8 additional variables, bringing the total to 70. Our results are summarized in tables 3 and 4, which list all of the confirmed variable stars in our field of view.

We found 37 RRab and 14 RRc variables within a 15.8×15.8 arcmin field centred at the coordinates of NGC 6401. Of these, 23 RRab and 11 RRc are within one cluster radius¹⁰ ($2.4'$) from the centre of NGC 6401 and most likely belong to the cluster. Finding charts are provided in Figures 3 and 4. The variable light curves for the likely cluster members are displayed in Figures 5 and 6, and their locations on the CMD are shown in Figure 2. The light curves of other variables are plotted in Figures A1 and A2.

Cluster variables listed in table 3 are denoted by the letter V, with all numbers up to 25 belonging to the Terzan & Rutily lists. OGLE identifiers, where available, are also provided in the second column. Our best fit periods and the OGLE periods are given

¹⁰ The list of all 158 globular clusters in the Milky Way is available at http://messier.obspm.fr/xtra/supp/mw_gc.html

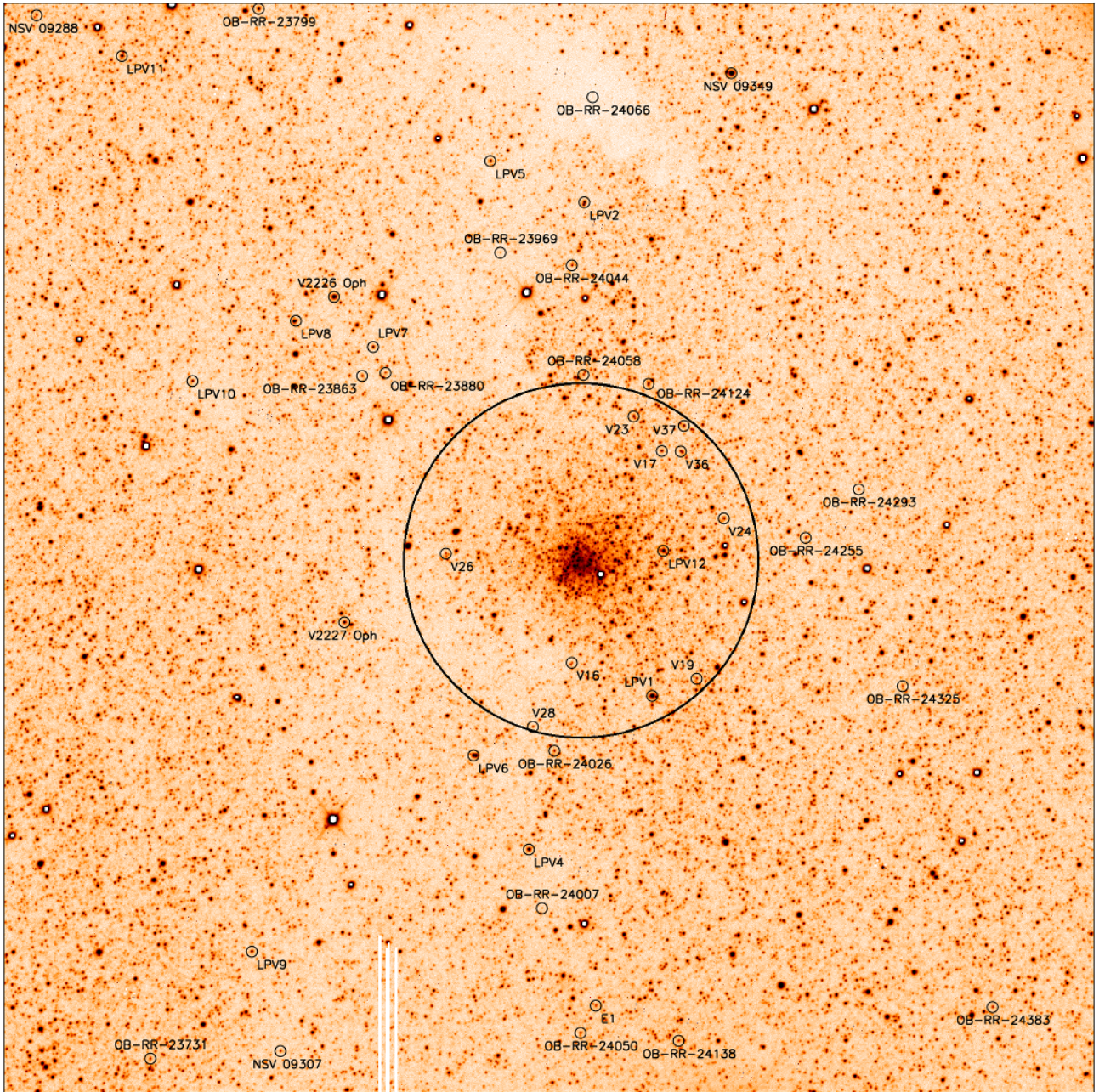


Figure 3. Finding chart constructed from our SDSS- g' band reference image. North is up and East is to the right. The cluster image is 15.8×15.8 arcmin². All of the confirmed variables in our FoV are identified, except in the crowded cluster core (see Figure 4). The circle marks the cluster radius of $2.4'$. OGLE variable names have been abbreviated for clarity.

in columns four and five respectively. Non-member variables are listed in Table 4, which includes 17 long period variables (LPV) with periods > 27 days. Their light curves are displayed in the Appendix. Long period variables (LPV) 1 to 12 are new discoveries. We note that the shape of the light curve of variable V3 suggests that it is most likely a W Virginis (CWB) star with a period of ~ 1.75 days. The eclipsing binary E1 is also a new discovery. All light curves are available for download in the electronic version of this article. An excerpt from the full table of electronic data is provided in Table 2.

3.2 The case of variable V12

We detected two independent frequencies in the SDSS- g' and SDSS- i' light curves of the RR Lyrae. The frequency spectra are shown in Figure 7. The top panels show the prominent peaks, which alternate in intensity between the g -band and the i -band case. Pre-whitening the strongest peak leads to the spectra shown in the middle panels. In both cases the secondary peak persists, which demonstrates that these signals are not aliases of each other. Subsequent pre-whitening of the secondary peak removes all signals as seen in the bottom panels.

The frequency ratio of these two signals is 0.884, i.e., far from the canonical 0.745 expected if this star was a radial double

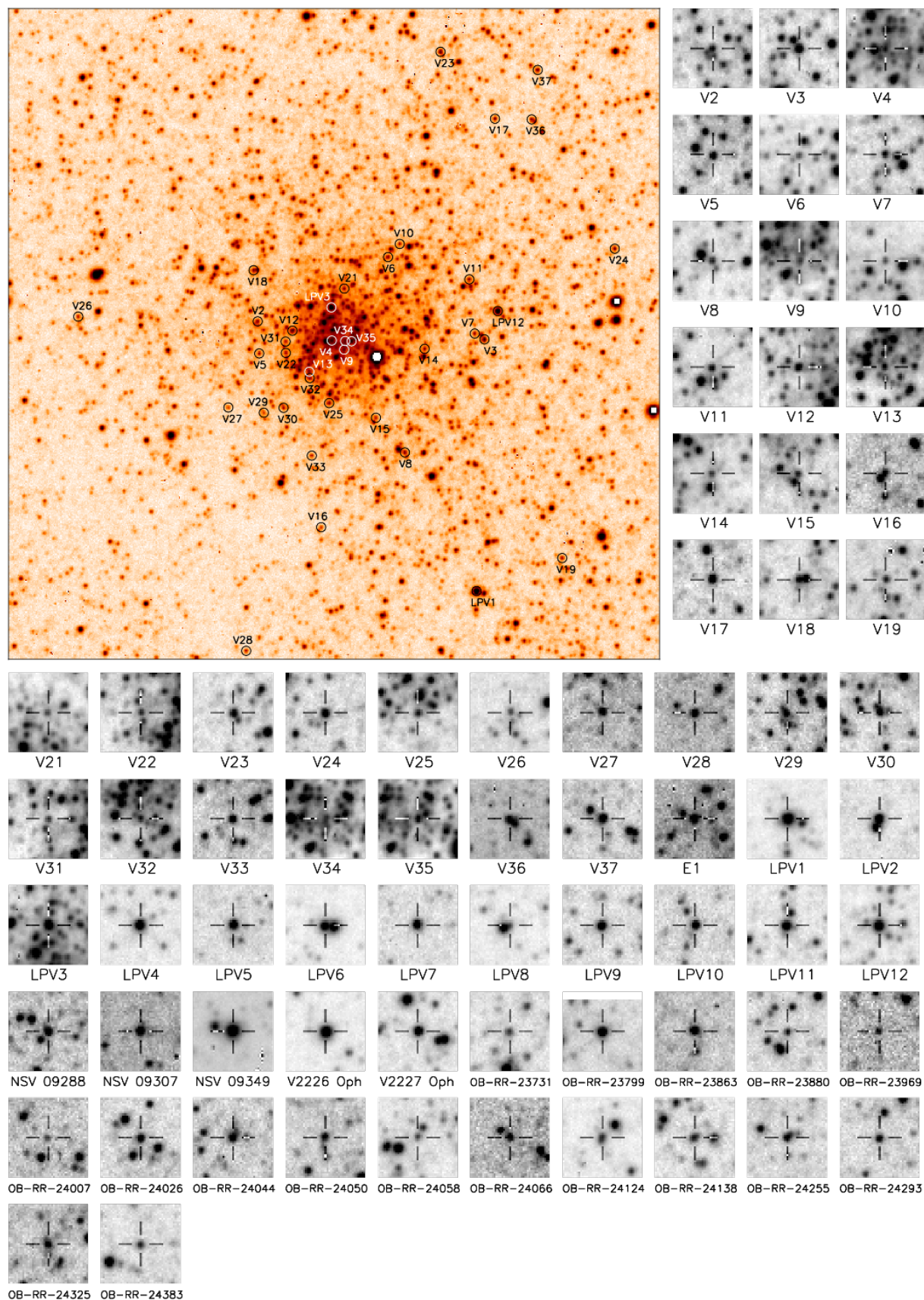


Figure 4. Finding chart constructed from our SDSS- g' band reference image covering the cluster region. North is up and East is to the right. The cluster image is 4.8×4.8 arcmin². All of the confirmed variables in this sub-field are identified. The image stamps are of size 19.3×19.3 arcsec². Each confirmed variable lies at the centre of its corresponding image stamp and is marked by a cross-hair. Image stamps are presented for all confirmed variables in our full FoV. Note that the image stamp for OB-RR-24066 is taken from our SDSS- i' band reference image instead, since it is not detected in the SDSS- g' band reference image. OGLE variable names have been abbreviated for clarity.

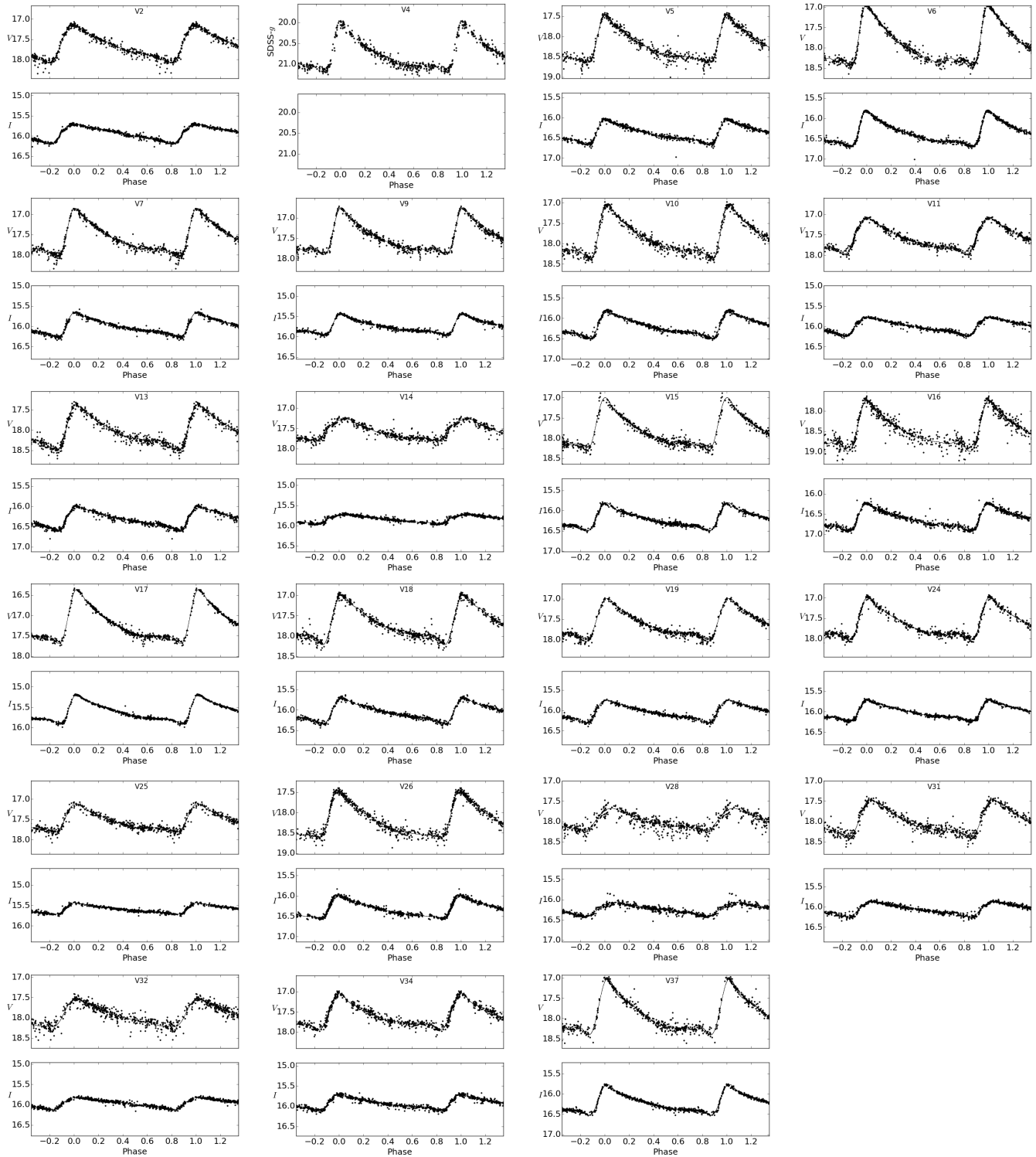


Figure 5. Standard SDSS- g' and SDSS- i' band light curves, linearly transformed to the V and I bands respectively, for the RRab stars in NGC 6401 phased with the periods listed in column 5 of Table 3 (or column 4 if no OGLE period was available). Note that no SDSS- i' band data were available for V4 due to its proximity to a bad pixel region on the CCD so only SDSS- g' band instrumental magnitudes are displayed.

mode pulsator RR01 (RRd) (fundamental-first overtone) or 0.80 for RR12 stars (first and second overtone modes). No RR12 have yet been identified in globular clusters but three were detected by Alcock et al. (2000) in the Large Magellanic Cloud (LMC). From

this we may conclude that in the case of V12 either one or both pulsation modes are non-radial.

Other non-radial pulsators among first overtone or RR1 RR Lyraes have been identified in the globular cluster M55 (Olech et al. 1999) and by (Alcock et al. 2000) in the LMC. The fundamen-

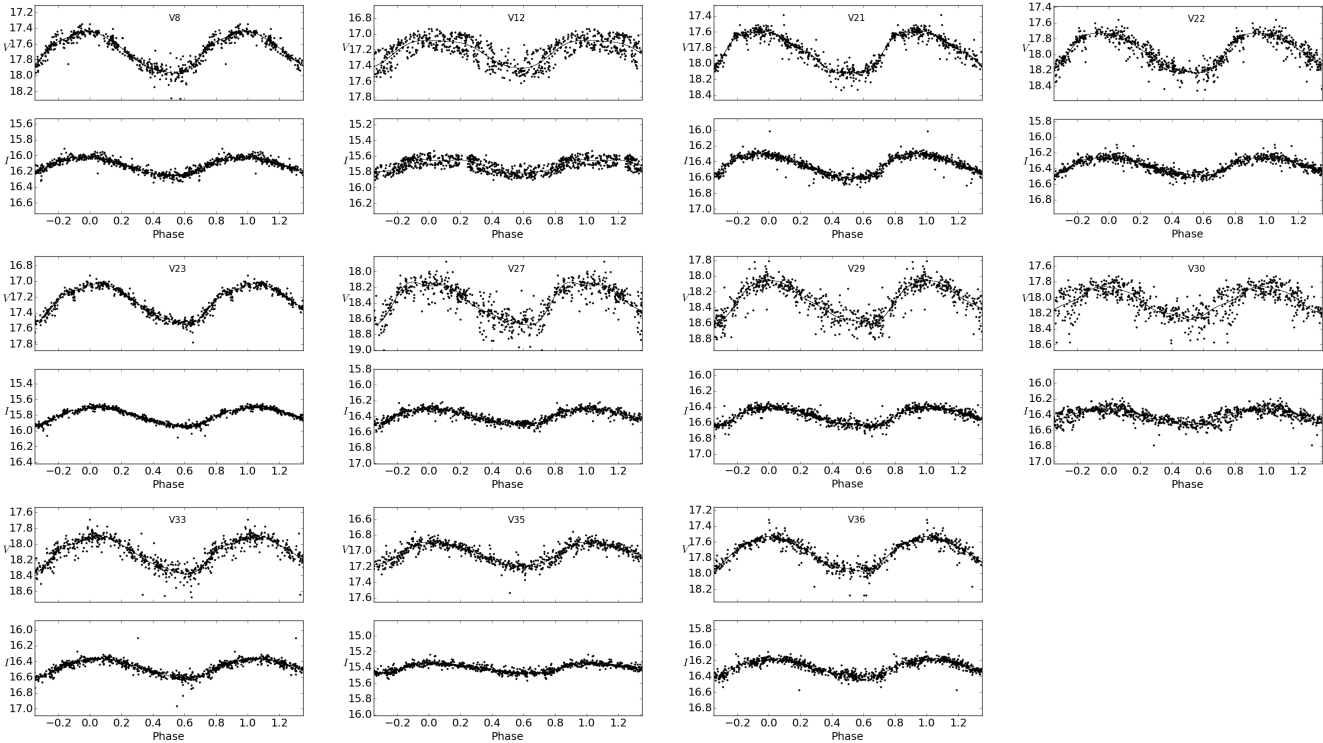


Figure 6. Standard SDSS- g' and SDSS- i' band light curves, linearly transformed to the V and I bands respectively, for the RRc stars in NGC 6401 phased with the periods listed in column 5 of Table 3 (or column 4 if no OGLE period was available).

tal difference of V12 with all these non-radial pulsator RR Lyrae is that in all of them the frequency ratio is always larger than 0.95, whereas it is only 0.884 in V12. Thus V12 adds to the list of non-radial pulsator RR Lyrae stars in globular clusters. Precise determination of the excited non-radial mode would require abundant and accurate data.

4 DETERMINATION OF THE PHYSICAL PARAMETERS FROM THE RR LYR VARIABLES

We used Fourier decomposition of the calibrated SDSS- g' and SDSS- i' band RR Lyr light curves into their harmonics in order to estimate the metallicity, luminosity and effective temperature of the stars. Fourier decomposition involves modeling the light curves as a Fourier series of the form:

$$m(t) = A_0 + \sum_{k=1}^N A_k \cos \left[\frac{2\pi}{P} k(t - E) + \phi_k \right], \quad (5)$$

where $m(t)$ is the magnitude at time t , N the number of harmonics used in the fit, P the period of variability, and E the reference epoch. A_k and ϕ_k are the amplitudes and phases of the sinusoidal components respectively. The fit to the data was performed using linear least squares, and the best fit values of the amplitudes and phases of the harmonics were evaluated. From these, the Fourier parameters $\phi_{ij} = j\phi_i - i\phi_j$ and $R_{ij} = A_i/A_j$ were determined. In order to avoid fitting noise in the data, each variable was modeled with the lowest possible number of harmonics. We note that, where available, we used the OGLE data to refine the estimates of the periods during the fitting process.

Since our observations were originally in the SDSS- g' and

SDSS- i' bands, we performed our fits in each band using the alternative Fourier form:

$$m(t) = A_0 + \sum_{k=1}^N B_k \cos \left[\frac{2\pi}{P} k(t - E) \right] + C_k \sin \left[\frac{2\pi}{P} k(t - E) \right], \quad (6)$$

from which we derived the coefficients B_k and C_k . These Fourier coefficients were then converted to their equivalents in the V -band using the Lupton (2005) transformations between SDSS magnitudes and UBVRC combined with our equation 4, from which we derived $B_k(V) = 0.5778B_k(g) + 0.4222B_k(i)$ and $C_k(V) = 0.5778C_k(g) + 0.4222C_k(i)$. We then estimated the coefficients $A_k(V) = \sqrt{B_k(V)^2 + C_k(V)^2}$ and $\phi_k(V) = \cos^{-1}(B_k(V)/A_k(V))$.

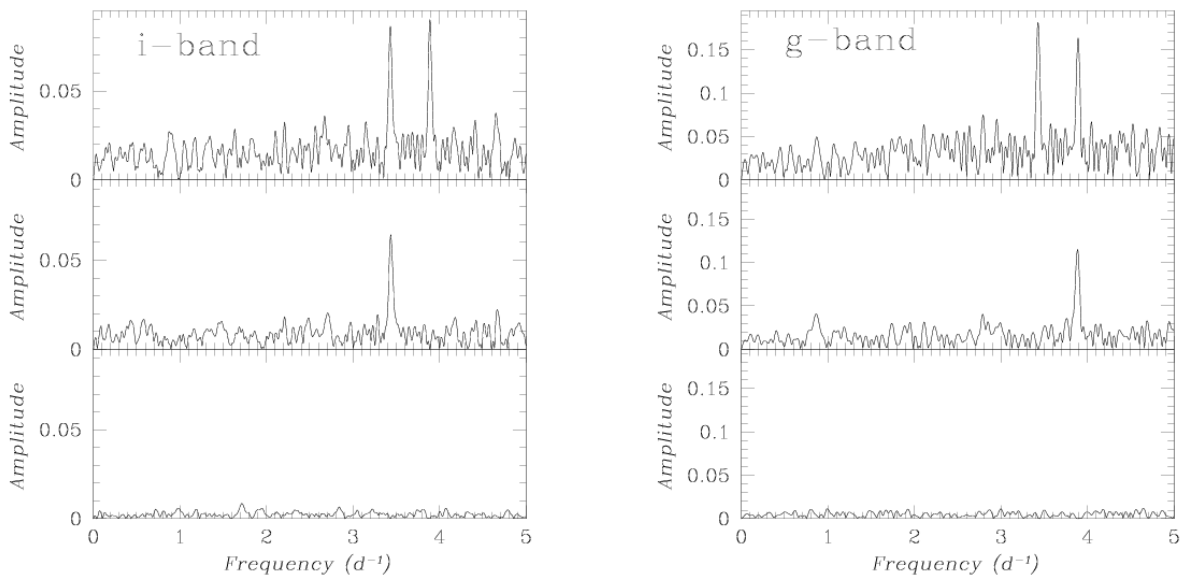
The best fit parameters and number of harmonics used for individual RRab and RRc variable light curves are listed in Table 5. Some variables did not provide useful constraints and were excluded from further analysis. Specifically, when determining the physical parameters, we did not use the following variables: V12 exhibits non-radial pulsation (see section 3.2); V30 shows too much scatter and its Fourier parameters are unreliable; V14 and V28 have a *deviation parameter*, defined by Jurcsik & Kovacs (1996), $D_m > 5.0$ and are therefore not suitable to use for calibration purposes. V4 was also not used because it has no SDSS- i' data.

4.1 Metallicity

The Fourier decomposition parameters of RRab stars can be used to calculate the metallicity from the semi-empirical relationships of Jurcsik & Kovács (1996), which express $[\text{Fe}/\text{H}]$ as a function of the period and Fourier parameter $\phi_{31}^{(s)}$, where the superscript s denotes

Table 5. Fourier decomposition parameters (*V*-band).

Star	A_0	A_1	A_2	A_3	A_4	ϕ_{21}	ϕ_{31}	ϕ_{41}	N	D_m
RRab stars										
V2	17.664	0.271	0.128	0.080	0.032	4.440	9.069	7.248	6	3.14
V5	18.234	0.323	0.160	0.111	0.065	3.953	8.313	6.350	7	1.52
V6	17.956	0.424	0.201	0.156	0.099	3.821	7.935	5.931	8	3.08
V7	17.598	0.307	0.165	0.110	0.072	3.984	8.391	6.479	8	2.39
V9	17.510	0.289	0.142	0.109	0.070	3.950	8.089	6.053	7	1.70
V10	17.878	0.344	0.176	0.124	0.083	3.972	8.323	6.321	9	2.86
V11	17.593	0.243	0.124	0.079	0.045	4.153	8.603	6.964	6	1.13
V13	18.037	0.292	0.163	0.105	0.064	4.102	8.596	6.779	7	3.18
V14	17.579	0.164	0.070	0.033	0.015	4.135	8.446	7.417	6	7.88
V15	17.839	0.336	0.172	0.123	0.078	3.948	8.221	6.197	6	1.81
V16	18.508	0.320	0.166	0.117	0.088	4.006	8.282	6.327	6	2.30
V17	17.217	0.358	0.174	0.130	0.081	3.901	8.158	6.143	7	1.01
V18	17.712	0.316	0.170	0.110	0.080	4.081	8.429	6.636	6	1.94
V19	17.625	0.282	0.147	0.097	0.060	4.065	8.495	6.692	6	1.15
V24	17.647	0.277	0.136	0.096	0.067	3.908	8.241	6.213	7	2.21
V25	17.549	0.184	0.090	0.061	0.035	4.009	8.423	6.678	7	3.41
V26	18.216	0.335	0.150	0.103	0.065	3.936	8.229	6.051	7	2.63
V28	17.999	0.170	0.082	0.041	0.018	4.144	8.607	7.232	7	5.37
V31	18.000	0.246	0.126	0.072	0.043	4.033	8.574	6.856	6	4.73
V32	17.941	0.201	0.094	0.047	0.020	4.328	8.983	7.103	6	2.72
V34	17.603	0.227	0.117	0.077	0.056	3.964	8.370	6.413	6	2.62
V37	17.928	0.370	0.173	0.126	0.096	3.844	8.138	6.007	6	1.89
RRc stars										
V8	17.707	0.205	0.015	0.013	0.007	5.002	4.222	2.888	4	—
V12	17.234	0.144	0.024	0.012	0.001	5.968	3.033	1.745	4	—
V21	17.861	0.226	0.035	0.015	0.020	4.758	2.985	1.830	4	—
V22	17.983	0.202	0.026	0.015	0.009	4.586	3.359	1.670	4	—
V23	17.279	0.196	0.015	0.016	0.010	5.029	4.357	3.074	4	—
V27	18.404	0.195	0.037	0.030	0.013	4.689	3.543	1.477	4	—
V29	18.344	0.205	0.039	0.015	0.014	4.408	3.193	2.263	4	—
V30	18.074	0.156	0.007	0.008	0.011	3.731	4.977	5.157	4	—
V33	18.131	0.185	0.018	0.016	0.010	5.075	4.747	3.342	4	—
V35	17.048	0.117	0.015	0.008	0.005	4.808	2.378	1.185	4	—
V36	17.756	0.174	0.016	0.012	0.009	4.477	3.908	3.005	4	—

**Figure 7.** Frequency spectra for V12 in the SDSS-*i'* (left) and SDSS-*g'* (right) bands.

a Fourier *sine* series. Since we used a *cosine* series for our fits (6), we converted to *sine* using $\phi_{ij}^{(s)} = \phi_{ij} - (i - j)\frac{\pi}{2}$.

The metallicity is then given by:

$$[\text{Fe}/\text{H}]_J = -5.038 - 5.394 P + 1.345 \phi_{31}^{(s)}, \quad (7)$$

where the subscript J denotes a non-calibrated metallicity. This can be converted to the metallicity scale of Zinn & West (1984) (hereafter ZW) using the following relationship from Jurcsik (1995):

$$[\text{Fe}/\text{H}]_{\text{ZW}} = \frac{[\text{Fe}/\text{H}]_J - 0.88}{1.431}. \quad (8)$$

Equation 7 is only applicable to RRab stars with a *deviation parameter* D_m below a given limit. Although Jurcsik & Kovacs (1996) originally used $D_m < 3.0$, some authors have relaxed that condition to $D_m < 5.0$ with the aim of improving the statistics of the mean physical parameters. We therefore adopted $D_m < 5.0$ as a selection criterion to estimate stellar properties for our RRab stars and have rejected stars V14 and V28 with $D_m > 5.0$ when estimating the physical parameters.

The metallicity can also be obtained for the RRc stars using $[\text{Fe}/\text{H}]_{\text{ZW}} = 52.466 P^2 - 30.075 P + 0.131 \phi_{31}^2 + 0.982 \phi_{31} - 4.198 \phi_{31} P + 2.424$, (9)

from Morgan et al. (2007) (her equation 3).

Metallicity values calculated using these relationships are reported in Tables 6 and 7. The transformation to the UVES (Carretta et al. 2009) scale is given by:

$$[\text{Fe}/\text{H}]_{\text{UVES}} = -0.413 + 0.130[\text{Fe}/\text{H}]_{\text{ZW}} - 0.356[\text{Fe}/\text{H}]_{\text{ZW}}^2. \quad (10)$$

The mean metallicities on the ZW scale for RRab and RRc stars are -1.254 ± 0.064 and -1.252 ± 0.210 respectively.

4.2 Effective Temperature

The Fourier parameters may also be used to estimate the effective temperature, T_{eff} , for RRab and RRc stars. For the RRab variables, we used the relationships derived by Jurcsik (1998), which link the $(V - K)_0$ colour to the period P :

$$\log(T_{\text{eff}}) = 3.9291 - 0.1112 (V - K)_0 - 0.0032 [\text{Fe}/\text{H}], \quad (11)$$

with

$$(V - K)_0 = 1.585 + 1.257 P - 0.273 A_1 - 0.234 \phi_{31}^{(s)} + 0.062 \phi_{41}^{(s)}. \quad (12)$$

For the RRc stars the calibration of Simon & Clement (1993) can be used:

$$\log(T_{\text{eff}}) = 3.7746 - 0.1452 \log(P) + 0.0056 \phi_{31}. \quad (13)$$

Note that the temperatures for RRab and RRc stars calculated using the relationships above are on different absolute scales. For a discussion of the accuracy and caveats of these calibrations we refer the reader to Cacciari et al. (2005), Arellano Ferro et al. (2008) and Bramich et al. (2011).

The mean effective temperature for the RRab stars is 6503.87 ± 78.37 K and for the RRc stars 7397.68 ± 49.23 K.

4.3 Absolute Magnitudes

For the RRab stars, we used Kovacs & Walker (2001) to derive the absolute magnitude

$$M_V = -1.876 \log P - 1.158 A_1 + 0.821 A_3 + K_0, \quad (14)$$

where the zero-point of the calibration is $K_0 = 0.41 \pm 0.02$ mag, as discussed in Kains et al. (2015).

For the RRc stars, equation 10 from Kovacs (1998) is used instead, after adopting the zero-point value $K_1 = 1.061 \pm 0.02$ mag used in Cacciari et al. (2005):

$$M_V = K_1 - 0.961 P - 0.044 \phi_{21}^{(s)} - 4.447 A_4. \quad (15)$$

The magnitudes were then converted to luminosities using

$$\log(L/L_\odot) = -0.4(M_V - M_{\text{bol},\odot} + B_C) \quad (16)$$

where $M_{\text{bol},\odot} = 4.75$ is the solar bolometric magnitude and $B_C = 0.06[\text{Fe}/\text{H}]_{\text{ZW}} + 0.06$ is the bolometric correction term given by Sandage & Cacciari (1990).

The mean absolute magnitudes for the RRab and RRc stars are 0.648 ± 0.062 and 0.576 ± 0.032 respectively.

4.4 Bailey Diagram and Oosterhoff Type

We could not find any assessment of the Oosterhoff type of NGC 6401 in the literature. Using the RR Lyrae variable stars listed in Table 3, we estimated mean periods $\langle P_{\text{RRab}} \rangle = 0.55 \pm 0.06$ days and $\langle P_{\text{RRc}} \rangle = 0.30 \pm 0.03$ days. We found that 68% of the RR Lyrae variables in the cluster are RRab's. These values and the derived metallicity of NGC 6401 indicate that the cluster is Oosterhoff type I (e.g. Clement et al. (2001)).

The SDSS- i' band Bailey diagram ($\log P$ versus A_i) for the cluster RR Lyrae variables is shown in Figure 8. Since RRab stars have longer periods and greater amplitudes than RRc stars, they occupy distinctly different areas on the figure. Solid and dashed lines mark the mean distributions of regular and evolved stars for Oosterhoff type I (OoI) and type II (OoII) clusters. The proximity of the NGC 6401 RRab and RRc locations to the lines corresponding to OoI clusters confirms our classification. We do not present the corresponding SDSS- g' band diagram since we have no comparison theoretical lines to display.

4.5 Correcting for extinction

As pointed out in Barbuy et al. (1999), NGC 6401 suffers from heavy differential reddening. Foreground reddening estimates at and around the cluster centre coordinates range from $E(B - V) = 0.53$ (Barbuy et al. 1999) to $E(B - V) = 1.1$ (Valenti, Ferraro & Origlia 2007), with multiple authors giving estimates in between those extremes (e.g. $E(B - V) = 0.85$ (Harris 1996; Piotto et al. 2002), 0.81 (Bica & Allain 1986; Schlafly & Finkbeiner 2011), 0.59 (Minniti 1995), 0.96 (Schlegel, Finkbeiner & Davis 1998)). These can be converted to $E(V - I)$ reddening values through $E(V - I) = 1.259E(B - V)$, derived from Schlegel, Finkbeiner & Davis (1998). In order to derive reasonable distances to the cluster, appropriate reddening calibrations need to be applied.

After taking into account small corrections for period and metallicity differences between stars, Sturch (1966) discovered that all RRab stars have nearly the same dereddened $(B - V)$ colour at minimum light (i.e. between the phase interval 0.5-0.8). Mateo et al. (1995) suggested that $(V - I)$ colour at minimum light is a better indicator of foreground reddening. This was confirmed by Day et al. (2002), who found that the mean dereddened $(V - I)$ colour at minimum light was 0.57 ± 0.025 mag, with little-to-no dependence on metallicity or period. This was further refined by Guldenschuh et al. (2005) to $(V - I)_{0,\text{min}} = 0.58 \pm 0.02$ mag, who also found no dependence on metallicity or pulsation amplitude. Guldenschuh

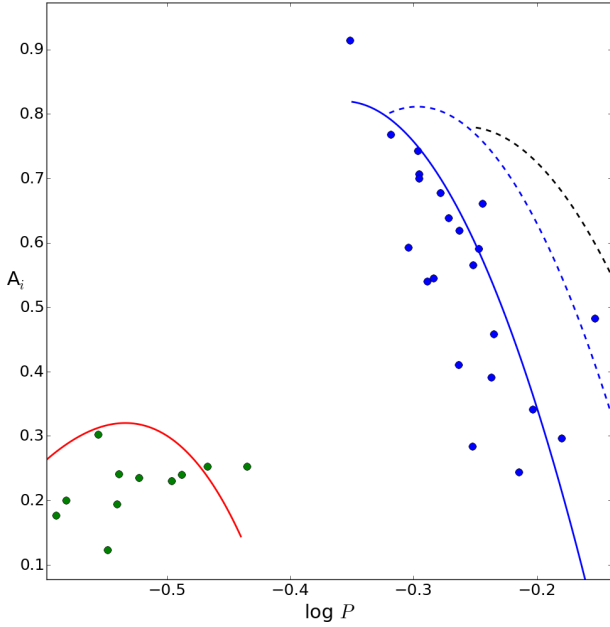


Figure 8. Period-amplitude distributions for the RR Lyrae stars in NGC 6401 in the SDSS- i' band. RRab and RRc stars are marked with blue and green circles respectively. The dashed black curve was calculated by Arellano Ferro et al. (2011, 2013) for the OoII clusters NGC 5024 and NGC 6333. The solid blue and dashed blue curves are from Kunder et al. (2013) for the OoI cluster NGC 2808 and correspond to the mean distributions of regular and evolved stars respectively. The red curve was calculated by Arellano Ferro et al. (2015) for a sample of RRc stars in five OoI type clusters.

also provided an independent colour-metallicity calibration in the form of $(V - I)_{0,\min} = 0.569 - 0.008[\text{Fe}/\text{H}]$, with an rms of 0.024 mag. Kunder & Chaboyer (2010) validated these relationships for RRab stars in the Galactic bulge.

To determine distances to individual RRab stars, we calculated the mean dereddened magnitudes using $I_0 = I - A_I$ and $V_0 = V - A_V$. The value for the extinction A_I was obtained using the relationships in Schlegel, Finkbeiner & Davis (1998):

$$A_I = 1.4626E(V - I), \quad (17)$$

and, again following Schlegel, Finkbeiner & Davis (1998), $A_V = 1.6835A_I$. The reddening in the optical is given by

$$E(V - I) = (V - I) - (V - I)_0, \quad (18)$$

where the color $(V - I)$ is evaluated from the observed RRab colour at minimum light, and $(V - I)_0$ is the intrinsic colour at minimum light $(V - I)_{0,\min} = 0.58$ mag. For comparison, we also provide the reddening values obtained using the following approximate formula from Kovacs & Walker (2001):

$$(V - I)_0 = 0.253\log(P) - 0.388A_1 + 0.364A_3 + 0.648. \quad (19)$$

The reddening values evaluated using the minimum light method are given in column 6 of Table 6 and those calculated via expression 19 in column 7.

4.6 Distance to NGC6401 using RR Lyrae stars

The absolute magnitude M_V can be used to determine the distance d to each RRab star using:

$$d = 10^{1+0.2(V_0 - M_V)}, \quad (20)$$

Table 6. Physical parameters for the RRab stars in NGC 6401. Stars marked with an asterisk (*) were not included when estimating averages. Column 6 lists the reddening calculated using the minimum light method, while column 7 lists the values obtained using equation 19.

Star	$[\text{Fe}/\text{H}]_{\text{ZW}}$	M_V	$\log(L/L_\odot)$	T_{eff}	$E(V - I)$	$E(V - I)$ [KW01]	Distance (kpc)
RRab stars							
V2	-1.212	0.450	1.725	6344.22	1.292	1.339	6.406
V5	-1.287	0.638	1.651	6522.05	1.405	1.491	6.720
V6	-1.305	0.708	1.624	6654.18	1.176	1.305	7.419
V7	-1.258	0.639	1.651	6504.83	1.146	1.224	6.726
V9	-1.419	0.709	1.627	6502.29	1.344	1.422	4.993
V10	-1.248	0.637	1.651	6552.30	1.249	1.340	6.808
V11	-1.196	0.634	1.651	6429.07	1.114	1.171	6.970
V13	-1.140	0.623	1.654	6498.34	1.257	1.327	7.306
V14*	-1.444	0.652	1.650	6250.92	1.248	1.286	5.899
V15	-1.270	0.676	1.636	6564.51	1.210	1.302	6.866
V16	-1.210	0.692	1.628	6565.09	1.424	1.512	7.278
V17	-1.325	0.659	1.644	6561.62	1.177	1.276	5.396
V18	-1.315	0.592	1.671	6460.35	1.218	1.294	6.670
V19	-1.213	0.636	1.651	6480.19	1.126	1.196	6.972
V24	-1.303	0.701	1.627	6517.09	1.183	1.259	6.407
V25	-1.277	0.722	1.618	6415.69	1.486	1.531	4.302
V26	-1.227	0.676	1.635	6599.57	1.469	1.570	6.088
V28*	-1.350	0.631	1.656	6295.70	1.249	1.284	7.219
V31	-1.210	0.631	1.653	6438.13	1.487	1.548	5.516
V32	-1.135	0.554	1.682	6375.44	1.508	1.546	5.430
V34	-1.277	0.704	1.625	6469.60	1.204	1.263	6.121
V37	-1.247	0.684	1.633	6622.74	1.269	1.379	6.667
Weighted	-1.254	0.648	1.647	6503.87	1.287	1.365	6.353
Mean	± 0.064	± 0.062	± 0.024	± 78.37	± 0.128	± 0.124	± 0.814

Table 7. Physical parameters for the RRc stars in NGC 6401. Stars marked with an asterisk (*) were not included when estimating averages.

Star	$[\text{Fe}/\text{H}]_{\text{ZW}}$	M_V	$\log(L/L_\odot)$	T_{eff}
RRc stars				
V8	-1.086	0.566	1.676	7398.51
V12*	-1.408	0.584	1.676	7403.00
V21	-1.269	0.566	1.680	7447.49
V22	-1.327	0.600	1.668	7402.74
V23	-1.489	0.514	1.706	7282.88
V27	-1.043	0.588	1.666	7464.05
V29	-1.282	0.598	1.668	7427.72
V30*	0.802	0.663	1.592	7707.52
V33	-0.911	0.536	1.683	7396.88
V35	-1.635	0.626	1.665	7370.81
V36	-1.226	0.587	1.671	7388.00
Weighted	-1.252	0.576	1.676	7397.68
Mean	± 0.210	± 0.032	± 0.012	± 49.23

where V_0 is the star's dereddened magnitude. We obtain a mean distance to the cluster $d \approx 6.35 \pm 0.81$ kpc. The derived distance is consistent with the value reported in Valenti, Ferraro & Origlia (2007) ($d \approx 7.7$ kpc) and significantly lower than the one found by Barbay et al. (1999) ($d \approx 12.0 \pm 1.0$ kpc). Our distances were estimated using the intrinsic colour at minimum light method.

5 DISCUSSION

This work presents the first detailed photometric time-series study of NGC 6401 employing CCD data. NGC 6401 is a little-investigated globular cluster 5.3° from the Galactic centre. It is

affected by strong differential reddening, which complicates photometric calibration, and hence the estimation of the physical parameters. This is possibly one of the reasons it has not been extensively studied in the past.

Using the RR Lyrae stars that are the most plausible cluster members, we have determined that NGC 6401 is an OoI cluster of intermediate metallicity that belongs to the metal-rich population of ~ 20 bulge clusters that lie within 2 kpc from the Galactic centre (Minniti 1995). Bica, Ortolani & Barbuy (2016) conclude that a cut-off of 3 kpc from the Galactic Centre is suitable in terms of isolating a bona-fide bulge cluster sample, with little contamination. As pointed out by Rossi et al. (2015), inner bulge globular clusters appear to be trapped in the bulge bar due to its high mass. This is very likely the case for NGC 6401 as well, since it is also in the bulge (Zoccali & Valenti 2016).

Forbes & Forte (2001) argue that the mean metallicity of globular clusters reveals information about the mass of the host galaxy because the chemical enrichment of globular clusters is directly linked to the galaxy formation process. In particular, they claim that the inner metal-rich globular clusters and the bulge field stars have similar colours because they formed at the same time from the same chemically enriched gas. Their findings agree with those of Barbuy, Bica & Ortolani (1998), who also conclude that bulge clusters share comparable properties with the bulge field stars, including not only metal-rich globular clusters, but also intermediate metallicity ones. In this work, we have derived independent metallicity and distance estimates for NGC 6401, which are compatible with the characteristics of other metal-rich globular clusters in the Galactic bulge. Our results provide further support to the idea that the bulge field stars and the inner globular cluster population evolved on the same timescales.

6 SUMMARY

We have updated the census of variable stars in NGC 6401. We use three different methods to recover 34 RR Lyrae cluster variables, three of which do not appear in the OGLE database (V8, V10 and V14). We do not find evidence of variability for the previously reported variables V1, V20 and OGLE-BLG-RRLYR-23724. We discovered 13 new variables, E1 and LPV1-12 and classified V3 as a W Virginis star for the first time. We detected double-mode non-radial pulsations in the RRc star V12, adding another example of these rare objects in globular clusters. Finally, we used the RR Lyrae content to establish that NGC6401 is an OoI type cluster.

The parameters obtained through Fourier decomposition of the light curves of a selected subset of RRab and RRc stars were used to estimate the metallicity, absolute magnitude, luminosity and effective temperature of each variable. The average metallicity for the cluster derived using the RRab stars $[\text{Fe}/\text{H}]_{\text{ZW}} = -1.25 \pm 0.06$ ($[\text{Fe}/\text{H}]_{\text{UVES}} = -1.13 \pm 0.06$) is consistent with that evaluated from the RRc stars $[\text{Fe}/\text{H}]_{\text{ZW}} = -1.25 \pm 0.21$ and lower than the estimate by Barbuy et al. (1999).

The mean distance to the cluster, estimated after individual RRab stars were corrected for differential reddening, is $d \approx 6.35 \pm 0.81$ kpc.

ACKNOWLEDGMENTS

We thank Igor Soszynski for providing calibrated OGLE light curves of stars in our field. This work made use of Python routines

based on gatspy and astroML methods. This project was supported by DGAPA-UNAM grant through project IN106615. D.M.B. acknowledges NPRP grant # X-019-1-006 from the Qatar National Research Fund (a member of Qatar Foundation). This work makes use of observations from the LCOGT network. This work has made a large use of the SIMBAD and ADS services.

REFERENCES

- Alard C., Lupton R. H., 1998, *ApJ*, 503, 325
 Alcock C., et al, 2000, *ApJ*, 542, 257
 Arellano Ferro A., Mancera Piña P. E., Bramich D. M., Giridhar S., Ahumada J. A., Kains N., Kuppuswamy K., 2015, *MNRAS*, 452, 727
 Arellano Ferro A., et al., 2013, *MNRAS*, 434, 1220
 Arellano Ferro, A., Figuera Jaimes, R., Giridhar, Sunetra, Bramich, D. M., Hernandez Santisteban, J. V., Kuppuswamy, K., 2011, *MNRAS*, 416, 2265
 Arellano Ferro A., Rojas Lopez V., Giridhar S., Bramich D. M., 2008, *MNRAS*, 384, 1444
 Barbuy B., Ortolani S., Bica E., Desidera S., 1999, *A&A*, 348, 783
 Barbuy B., Bica E., Ortolani S., 1998, *A&A*, 333, 117
 Bica E., Ortolani E., Barbuy B., 2016, *PASA*, 33, e028
 Bica E., Allain D., 1986, *A&AS*, 66, 171
 Blu T., Thevenaz P., Unser M., 2001, *IEEE Trans. Image Processing*, 10, 1069
 Bramich D. M., Bachelet, E., Alsubai, K. A., Mislis, D., Parley, N., 2015, *A&A*, 577, 108
 Bramich D. M., et al., 2013, *MNRAS*, 428, 2275
 Bramich D.M., Freudling W., 2012, *MNRAS*, 424, 1584
 Bramich D. M., Figuera Jaimes R., Giridhar S., Arellano Ferro A., 2011, *MNRAS*, 413, 1275
 Bramich D. M., 2008, *MNRAS*, 386L, 77
 Cacciari C., Corwin T.M., Carney B.W., 2005, *AJ*, 129, 267
 Cardelli J.A., Clayton G.C., Mathis J.S., 1989, *ApJ*, 345, 245
 Carretta E., Bragaglia A., Gratton R., D’Orazi V., Lucatello S., 2009, *A&A*, 508, 695
 Clement C. M., et al., 2001, *AJ*, 122, 2587
 Davidge T. J., 2001, *AJ*, 121, 3100
 Day, A.S., et al., 2002, *PASP*, 114, 645
 Draper P.W., 2000, in Manset N., Veillet C., Crabtree D., eds. *ASP Conf. Ser. Vol. 216, Astronomical Data Analysis Software and Systems IX*. Astron. Soc. Pac., San Francisco, p. 615
 Figuera Jaimes R., Arellano Ferro A., Bramich D. M., Giridhar S., Kuppuswamy K., 2013, *A&A*, 556, 20
 Forbes, D. A., Forte, J. C., 2001, *MNRAS*, 322, 257
 Guldenschuh, K. A., et al. 2005, *PASP*, 117, 721
 Harris W.E., 1996, *AJ*, 112, 1487
 Ivezić Z., et al. 2007, *AJ*, 134, 973
 Jurcsik J., 1995, *Act. Astron.*, 45, 653
 Jurcsik J., Kovacs, G. 1996, *A&A*, 312, 111
 Jurcsik J., 1998, *A&A*, 333, 571
 Kains N., et al., 2015, *A&A*, 578, 128
 Kovács, G., Walker, A. R., 2001, *A&A* 371, 579
 Kovács, G., 1998, *MmSAI* 69, 49
 Kunder, A., et al., 2013, *AJ*, 146, 119
 Kunder, A., Chaboyer, B., 2010, *AJ*, 139, 415
 Lupton, R., 2005, <http://classic.sdss.org/dr4/algorithms/sdssUBVRITransform.html>
 Mateo, M., Udalski, A., Szymanski, M. Kaluzny, J., Kubiak, M., Krzemiński, W., 1995, *AJ*, 109, 588

- Minniti, D., 1995, *AJ*, 109, 4
Minniti, D., 1995, *A&A*, 303, 468
Morgan S.M., Wahl J.N., Wieckhorst R.M., 2007, *MNRAS*, 374, 1421
Olech A., Kaluzny J., Thompson I.B., Pych W., Krzeminski W., Schwarzenberg-Czerny A., 1999, *ApJ*, 118, 452
Pal Andras, Bakos Gaspar A., 2006, *PSP*, 118, 1474
Piotto G. et al., 2002, *A&A*, 391, 945
Rossi L. J., Ortolani S., Barbuy B., Bica E., Bonfanti A., 2015, *MNRAS*, 450, 3270
Samus N. N., Goranskij V. P., Durevich O. V., Kazarovets E. V., Kireeva N. N., Pastukhova E. N., Zharova A. V., 2009, *VizieR Online Data Catalog*, 1, 2025
Samus N. N., Kazarovets E. V., Pastukhova E. N., Tsvetkova, T. M., Durevich, O. V., 2009, *PASP*, 121, 1378
Sandage A., Cacciari C., 1990, *ApJ*, 350, 645
Schlafly E.F., Finkbeiner D.P., 2011, *ApJ*, 737, 103
Schlegel D.J., Finkbeiner D.P., Davis M., 1998, *ApJ*, 500, 525
Simon N. R., Clement C. M., 1993, *ApJ*, 410, 526
Stetson, Peter, B., 1987, *PASP*, 99, 191
Sturch C., 1966, *ApJ*, 143, 774
Soszynski I. et al., 2014, *AcA*, 64, 177
Terzan A., Rutily B., 1975, *A&A*, 38, 307
Terzan A., Rutily B., 1973, *IAU Colloq. 21: Variable Stars in Globular Clusters and in Related Systems*, 68
Terzan A., Rutily B., 1972, *A&A*, 16, 408
Tsapras Y. et al., 2009, *AN*, 330, 4
Udalski A., Szymanski M. K., Szymanski G., 2015, *AcA*, 65, 1
Udalski A., 2003, *AcA*, 53, 291
Valenti, E., Ferraro, F.R., Origlia, L., 2007, *AJ*, 133, 1287
Zacharias N., Finch C.T., Girard T.M., Henden A., Bartlett J.L., Monet D.G., Zacharias M.I., 2012, *AJ*, 145, 44
Zinn, R., West, M.J., 1984, *ApJS*, 55, 45
Zoccali M., Valenti E., 2016, *PASA*, 33, 25

¹Astronomisches Rechen-Institut, Zentrum für Astronomie der Universität Heidelberg (ZAH), 69120 Heidelberg, Germany.

²Instituto de Astronomía, Universidad Nacional Autónoma de México. Ciudad Universitaria CP 04510, Mexico.

³Qatar Environment and Energy Research Institute(QEERI), HBKU, Qatar Foundation, Doha, Qatar.

⁴European Southern Observatory, Karl-Schwarzschild-Straße 2, 85748 Garching bei München, Germany.

⁵SUPA, School of Physics and Astronomy, University of St. Andrews, North Haugh, St Andrews, KY16 9SS, United Kingdom.

⁶Space Telescope Institute, 3700 San Martin Drive, Baltimore, MD 21218, USA.

⁷Las Cumbres Observatory Global Telescope Network, 6740 Cortona Drive, suite 102, Goleta, CA 93117, USA.

⁸Niels Bohr Institute & Centre for Star and Planet Formation, University of Copenhagen, Øster Voldgade 5, 1350 - Copenhagen K, Denmark.

⁹Planetary and Space Sciences, Department of Physical Sciences, The Open University, Milton Keynes, MK7 6AA, UK.

¹⁰Max Planck Institute for Solar System Research, Max-Planck-Str. 2, 37191 Katlenburg-Lindau, Germany.

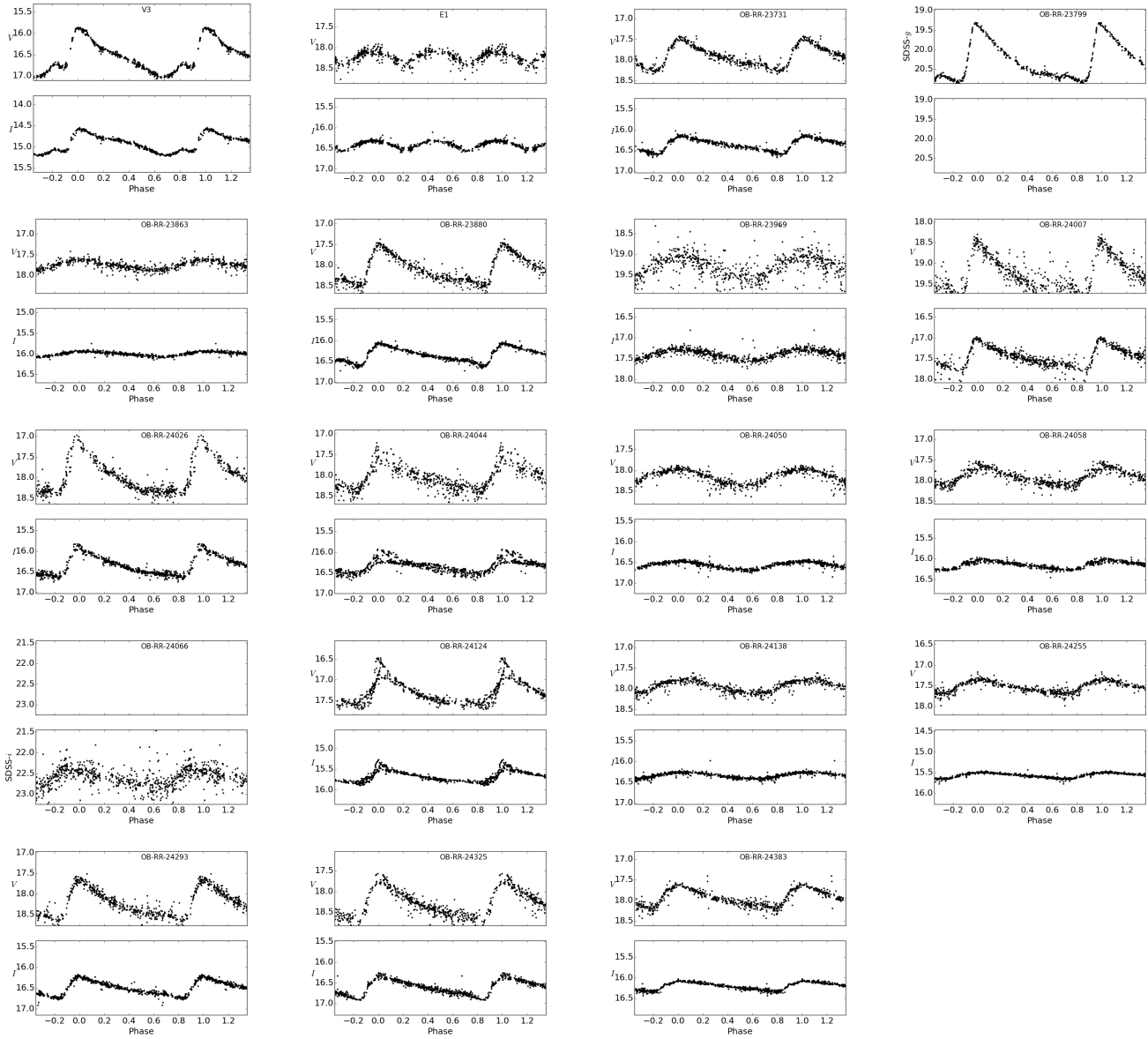


Figure A1. Standard SDSS- g' and SDSS- i' band light curves, linearly transformed to the V and I bands respectively, for V3, E1 and the RR Lyrae variable stars listed in Table 4. Note that no SDSS- i' band data were available for OB-RR-23799 so only SDSS- g' band instrumental magnitudes are displayed, and vice versa for OB-RR-24066.

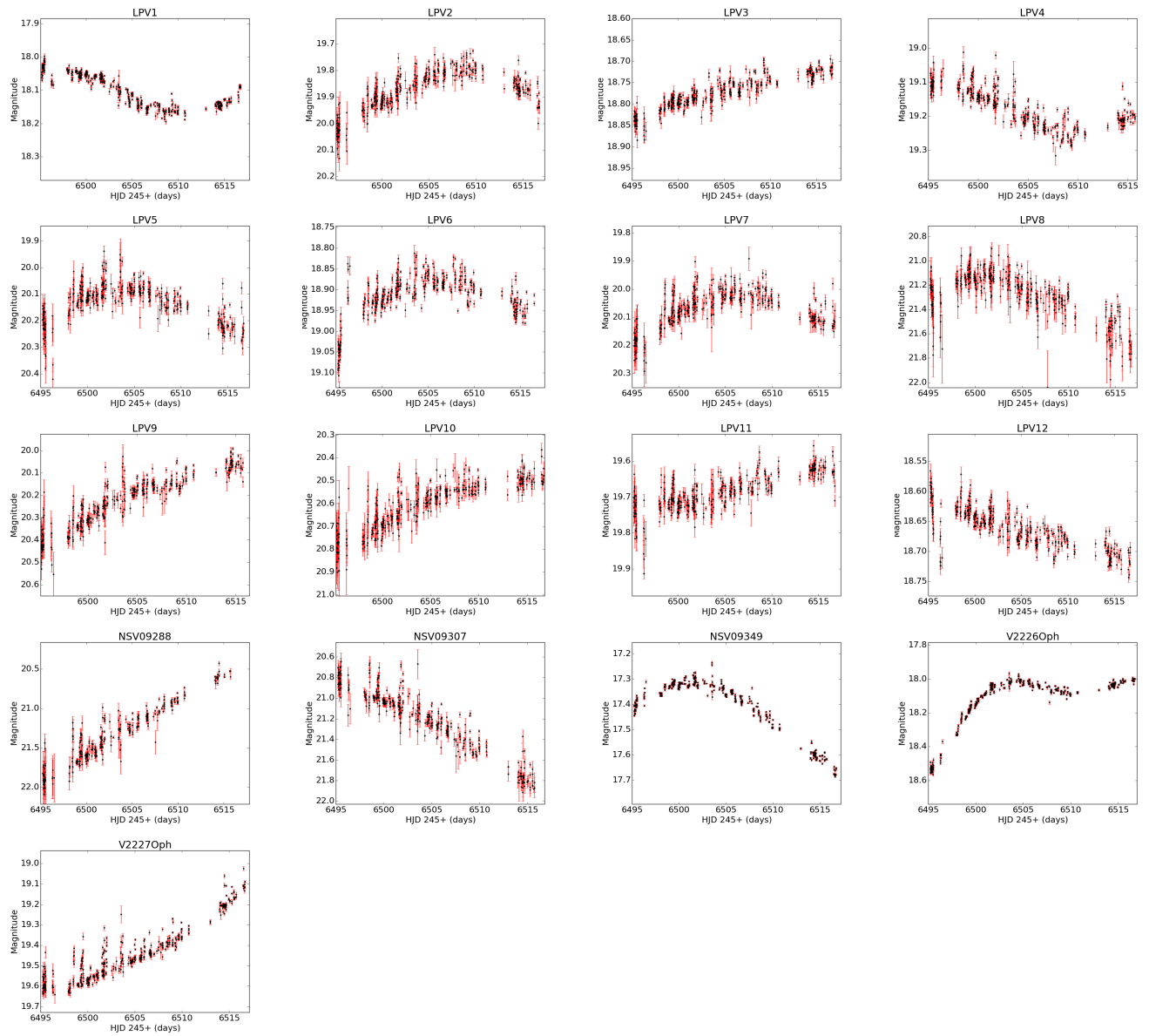


Figure A2. Light curves of the long period variable stars listed in Table 4. The reported magnitudes are in the instrumental SDSS- g' scale.